

SUPERPOSITION OF MULTI-VALUED SOLUTIONS IN HIGH FREQUENCY WAVE DYNAMICS

HAILIANG LIU AND ZHONGMING WANG

ABSTRACT. The weakly coupled WKB system captures high frequency wave dynamics in many applications. For such a system a level set method framework has been recently developed to compute multi-valued solutions to the Hamilton-Jacobi equation and evaluate position density accordingly. In this paper we propose two approaches for computing multi-valued quantities related to density, momentum as well as the energy. Within this level set framework we show that physical observables evaluated in [16, 15] are simply the superposition of their multi-valued correspondents. A series of numerical tests is performed to compute multi-valued quantities and validate the established superposition properties.

CONTENTS

1.	Introduction	1
2.	Review of Level Set Formulation and Computation of Averaged Density	4
2.1.	Level set formulation for velocity	4
2.2.	Level set formulation for both velocity and phase	4
2.3.	Evaluation of averaged density	5
3.	Computation of Multi-valued Density	5
4.	Superposition	6
5.	Numerical Implementation	7
6.	Numerical Examples	10
6.1.	The Schrödinger equation	10
6.2.	Wave equation	16
	Appendix	21
	Acknowledgments	24
	References	24

1. INTRODUCTION

We consider the WKB system of the form

$$(1.1) \quad \partial_t S + H(x, \nabla_x S) = 0, \quad t \in \mathbb{R}^+, \quad x \in \mathbb{R}^n,$$

$$(1.2) \quad \partial_t \rho + \nabla_x \cdot (\rho \nabla_p H(x, \nabla_x S)) = 0, \quad p = \nabla_x S \in \mathbb{R}^n,$$

subject to the initial data

$$(1.3) \quad S(0, x) = S_0(x),$$

$$(1.4) \quad \rho(0, x) = \rho_0(x).$$

Here $H(x, p)$ is called Hamiltonian, S denotes phase and ρ is position density. This nonlinear system arises in many contexts such as semi-classical approximations of the

Schrödinger equation

$$(1.5) \quad i\epsilon\partial_t\psi + \frac{\epsilon^2}{2}\Delta_x\psi = V(x)\psi,$$

and high frequency approximations of wave dynamics for hyperbolic equations such as

$$(1.6) \quad \partial_{tt}u - c^2(x)\Delta_x u = 0.$$

The main computational challenge for high frequency wave propagation problems is that the wave field is highly oscillatory, making direct simulation unrealistic. The WKB approximation is a classical way to approximate the wave field through an effective phase and a position density. The WKB system (1.1), (1.2) is formally derived from applying the following ansatz

$$(1.7) \quad A(t, x) \exp\left(\frac{iS(t, x)}{\epsilon}\right),$$

to the original wave equation, see e.g. [32]. The system (1.1) and (1.2) is weakly coupled, thus the effective phase S can be solved from the Hamilton-Jacobi equation, independent of the density. However, the nonlinearity of the Hamiltonian often leads to kinks in phase at finite time, which forces unbounded density to appear. The classical viscosity solutions [5, 18] are not adequate in describing the wave behavior beyond singularity, where multi-valued solutions in physical space should be considered.

Computation of multi-valued solutions is challenging, there has appeared a bulk of numerical methods to address the difficulty, ranging from Lagrangian methods, Hamilton-Jacobi equation based methods to kinetic formulation based methods. We refer to [7] for a seminal survey on computational high-frequency wave propagation. Recently, a new level set method framework has been developed for computing multi-valued phases and other physical observables in the entire physical domain in [4, 17, 19, 16, 15]; main development has been summarized in the review article [20]. A key idea is to represent the n -dimensional bi-characteristic manifold of the Hamilton-Jacobi equation in phase space by an implicit vector level set function $\Phi(t, x, p)$, whose components solve the same Liouville equation

$$\partial_t\Phi + \nabla_p H \cdot \nabla_x \Phi - \nabla_x H \cdot \nabla_p \Phi = 0, \quad \Phi_0 = p - \nabla_x S_0.$$

The multi-valued velocity $\{u_i(x, t)\}$ is realized by the zero level set, i.e.,

$$u_i(t, x) \in \{p, \quad \Phi(t, x, p) = 0\}$$

for $(t, x) \in R^+ \times R$.

The amplitude is hence evaluated by

$$\bar{\rho} = \int f\delta(\Phi)dp,$$

where the quantity f also solves the same Liouville equation with ρ_0 as initial data. Such a level set method is simple to implement, as accurate as the Lagrangian method [3], and in high dimensions more robust than the moment methods [2, 6, 9, 14]. Also the computation cost in the phase space can be reduced by using the local level set method [23, 24, 26].

Recently a field space based level set method is developed in [21, 22] for computing multi-valued velocity and electric fields governed by 1D Euler-Poisson equations

$$\begin{aligned}\partial_t \rho + \partial_x(\rho u) &= 0, \\ \partial_t + u \partial_x u &= E, \\ k E_x &= \rho - c.\end{aligned}$$

In particular, multi-valued density is computed from

$$\rho_i \in \left\{ \frac{f}{\left| \det \left(\frac{\partial(\phi_1, \phi_2)}{\partial(p, q)} \right) \right|} \Big| \phi_1 = 0, \phi_2 = 0 \right\},$$

where ϕ_1, ϕ_2 are two level set functions needed to determine both multi-valued velocity u and electric field E , and f solves the same level set equation in field space (x, p, q) , subject to the given initial density ρ_0 . It was shown that a superposition of these multi-valued density gives the averaged density over the level set manifold. Note that the obtained density from this formula will become unbounded wherever $\frac{\partial(\phi_1, \phi_2)}{\partial(p, q)}$ becomes zero, which corresponds to the density concentration near focus of particle paths. This phenomenon is verified by the sharp peaks in numerical examples.

The aim of this paper is to compute multi-valued quantities related to density, momentum and energy, and conduct numerical comparison with the averaged physical observables evaluated in [16, 15]. Following [22], we shall compute multi-valued density of the WKB system either by

$$(1.8) \quad \rho_i \in \left\{ \frac{f}{\left| \det(\nabla_p \Phi) \right|} \Big| \Phi(t, x, p) = 0 \right\},$$

or

$$(1.9) \quad \rho_i \in \left\{ \frac{\rho_0(\alpha)}{\left| \det \left(\frac{\partial x(t, \alpha)}{\partial \alpha} \right) \right|} \Big| x = x(t, \alpha) \right\},$$

where $x(t, \alpha)$ denotes the deformation map satisfying $\frac{dx}{dt} = \nabla_p H(x, p)|_{p=\nabla_x S}$ with $x(t, 0) = \alpha$. As remarked above, these two formulas are valid both before and after the caustics.

Within the level set framework we prove that the averaged density $\bar{\rho}$ is simply a linear superposition of multi-valued density, i.e.

$$\bar{\rho}(t, x) = \sum_{i=1}^N \rho_i(t, x),$$

where ρ_i is the i^{th} branch of multi-valued density ($1 \leq i \leq N$). Similar superposition properties are shown to also hold for other quantities such as momentum and energy. These properties are confirmed by a series of numerical examples.

We now conclude this section by outlining the rest of this paper. In Section 2 we review the level set framework introduced in [4, 17, 16], to compute multi-valued velocity, phase and averaged density of the system (1.1) and (1.2), since our results are based on the formulation derived therein. In Section 3 we discuss two techniques for computing the multi-valued density, one by the level set method, and another by the Lagrangian method. Superposition properties for multi-valued density, momentum as well as energy

are established in Section 4. Numerical procedures are detailed in Section 5. Finally, in Section 6 a series of numerical examples is presented to compute multi-valued observables and validate the superposition properties. Justification of the formula (1.9) is given in the Appendix.

2. REVIEW OF LEVEL SET FORMULATION AND COMPUTATION OF AVERAGED DENSITY

2.1. Level set formulation for velocity. The classical way to compute the multi-valued solution is to use Lagrangian method, i.e., following the characteristics of the Hamilton-Jacobi equation (1.1),

$$(2.1) \quad \frac{dx}{dt} = \nabla_p H(x, p), \quad \frac{dp}{dt} = -\nabla_x H(x, p),$$

$$(2.2) \quad x(0) = \alpha, \quad p(0) = \nabla_x S_0(\alpha).$$

Here p is the moment variable in phase space, i.e., $p = \nabla_x S$.

Following [4], let $\Phi(t, x, p)$ be a global invariant of (2.1) in the (x, p) space, then

$$\frac{d}{dt} \Phi(t, x(t), p(t)) \equiv 0,$$

which gives the following level set formulation

$$(2.3) \quad \partial_t \Phi + \nabla_p H(x, p) \nabla_x \Phi - \nabla_x H(x, p) \nabla_p \Phi = 0.$$

Thus the multi-valued velocity is determined by the zero level set of Φ . Meanwhile, the initial condition could be chosen as

$$(2.4) \quad \Phi(0, x, p) = p - \nabla_x S_0(x).$$

Note that the choice of initialization is not unique, as long as the zero level set gives the initial phase gradient $\nabla_x S_0$. We will see in later sections that this choice (2.4) would simplify the post processing in the evaluation of density ρ . Moreover, since there will be no fattening in the equations considered, the kernel of Φ is finite when it is initially finite.

2.2. Level set formulation for both velocity and phase. In addition to the bi-characteristic system (2.1), we can have

$$(2.5) \quad \frac{dS(t, x)}{dt} = -H(x, p) + p \nabla_p H(x, p), \quad S(0, x) = S_0(x).$$

Similarly let $\Phi(t, x, p, q)$ be a global invariant in the (x, p, q) space with $q = S$ along zero level set, then

$$\frac{d}{dt} \Phi(t, x(t), p(t), q(t)) \equiv 0,$$

which becomes

$$(2.6) \quad \partial_t \Phi + \nabla_p H \cdot \nabla_x \Phi - \nabla_x H \cdot \nabla_p \Phi + (p \cdot \nabla_p H - H) \partial_q \Phi = 0.$$

The initial condition for $\Phi = (\phi_1, \phi_2, \dots, \phi_{n+1})^T$ could be chosen as

$$\begin{aligned} \phi_i(0, x, p, q) &= p_i - \partial_{x_i} S_0(x), \quad i = 1, 2, \dots, n \\ \phi_{n+1}(0, x, p, q) &= q - S_0(x). \end{aligned}$$

Here the necessity of doing computation in $2n+1$ -dimension space is to capture the phase S as well. However, as pointed out in [4], multi-valued phase can also be recovered in phase space by

$$S(t, x) \in \left\{ \tilde{S}(t, x, p) \mid \Phi(t, x, p) = 0 \right\},$$

where the level set function Φ is solved from (2.3), and \tilde{S} solves

$$\begin{aligned} \partial_t \tilde{S} + \nabla_p H \cdot \nabla_x \tilde{S} - \nabla_x H \cdot \nabla_p \tilde{S} &= p \cdot \nabla_p H - H, \\ \tilde{S}(0, x, p) &= S_0(x). \end{aligned}$$

2.3. Evaluation of averaged density. Let f be the Liouville equation solving

$$(2.7) \quad f_t + \nabla_p H \cdot \nabla_x f - \nabla_x H \cdot \nabla_p f = 0, \quad f_0 = \rho_0.$$

Then the average density can be determined by

$$(2.8) \quad \bar{\rho}(t, x) = \int_{\mathbb{R}^n} f \delta(\Phi) dp.$$

Note that the momentum \bar{J} and energy \bar{E} can be evaluated by

$$(2.9) \quad \bar{J} = \int_{\mathbb{R}^n} H_p(x, p) f \delta(\Phi) dp,$$

$$(2.10) \quad \bar{E} = \int_{\mathbb{R}^n} H(x, p) f \delta(\Phi) dp.$$

3. COMPUTATION OF MULTI-VALUED DENSITY

As is known, the position density also becomes oscillatory as $\epsilon \rightarrow 0$. The averaged one may be regarded as the weak limit of position density. We shall now show how to compute the multi-valued density to the WKB system through this level set approach.

Let L be a Liouville operator given by

$$L := \partial_t + \nabla_p H \cdot \nabla_x - \nabla_x H \cdot \nabla_p,$$

and $\tilde{\rho}$ be a representation of $\rho(t, x)$ in phase space with $\tilde{\rho}(t, x, \nabla_x S) = \rho(t, x)$ and $J = \det(\nabla_p \Phi)$, then it is shown in [16] that

$$(3.1) \quad L(\tilde{\rho}|J|) \equiv 0.$$

From (2.7), we have

$$(3.2) \quad L(f) = 0, \quad f_0 = \rho_0.$$

This shows that f and $\tilde{\rho}|J|$ satisfies the same Liouville equation with the same initial condition ($|J_0| = 1$). Therefor uniqueness leads to

$$(3.3) \quad f = \tilde{\rho}|J|.$$

Hence, we can determine multi-valued density by

$$(3.4) \quad \rho_i \in \left\{ \frac{f}{|\det(\nabla_p \Phi)|} \mid \Phi(t, x, p) = 0 \right\}.$$

Once we solve (2.3) and (2.7), we will be able to find ρ_i using (3.4). We point out that the formula (3.4) is used after system develops multi-valued solutions.

Here, we summarize the computation of multi-valued density in general setting using the following pseudo-algorithm:

1. Solve the level set equation (2.3) for Φ and equation (2.7) for f .
2. Computation of $\det(\nabla_p \Phi)$. Note that the size of $\nabla_p \Phi$ is $n \times n$ and it is very efficient to evaluate the determinant for $n = 1, 2, 3$.
3. Evaluate the quantity $\frac{f}{|\det(\nabla_p \Phi)|}$ on zero level set of Φ .

The above approach works in all setting and it is sometimes more convenient to adopt an easier approach in specific cases.

Recalling the ODE system (2.1), if we can solve x and p in terms of t and α explicitly, we could use another Lagrangian approach to evaluate multi-valued density. By defining

$$(3.5) \quad \Gamma(t, \alpha) = \nabla_\alpha x,$$

we could find density by the following parameterized solution

$$(3.6) \quad \rho(t, x(t, \alpha)) = \frac{\rho_0(\alpha)}{|\det(\Gamma)|}.$$

The justification of this formula is seen in the Appendix of this paper.

4. SUPERPOSITION

Theorem 4.1 (Superposition Principle for $\bar{\rho}$). *Let $\{\rho_i\}_{i=1}^N$ be multi-valued densities corresponding to multi-valued velocity u_i determined by*

$$u_i \in \{p \mid \Phi(t, x, p) = 0\},$$

and

$$\bar{\rho} = \int f \delta(\Phi) dp,$$

where f solves (2.7) and Φ solves (2.3) with initial condition (2.4).

Then

$$(4.1) \quad \bar{\rho}(t, x) = \sum_{i=1}^N \rho_i(t, x).$$

Proof. First note that here u_i denotes i^{th} branch of multi-valued u instead of i^{th} component of vector u . In order to evaluate the integral (4.1), we assume that all (u_i) lie in a bounded domain. Use a partition of unity, $\sigma_i \in C_0^\infty$ vanishes near u_i , with $\sigma_i(u_i) = 1$ and $\sum \sigma_i = 1$, we have

$$\int_{\mathbb{R}^n} f \delta(\Phi) dp = \sum_{i=1}^N \int_{\mathbb{R}^n} f \sigma_i \delta(\Phi) dp.$$

It suffices to evaluate $\int f \sigma_i \delta(\Phi) dp$.

Recall that

$$\delta(\Phi(t, x, p)) = \frac{\delta(p - u_i)}{|\nabla_p \Phi(t, x, u_i)|}$$

wherever $|\nabla_p \Phi(t, x, u_i)|$ is nonzero.

Finally, by (3.3), we have

$$(4.2) \quad f(t, x, u_i) = \tilde{\rho}(t, x, u_i) |J|.$$

Thus near each u_i -support(u_i), we have

$$(4.3) \quad \begin{aligned} \bar{\rho}(t, x) &= \int_{\mathbb{R}^n} \sigma_i f \delta(\Phi) dp = \int_{\text{support}(u_i)} \tilde{\rho} |J| \frac{\delta(p - u_i)}{|J|} dp, \\ &= \tilde{\rho}(t, x, u_i) = \rho_i(t, x). \end{aligned}$$

This, combined with the partition of unity, gives the asserted (4.1). \square

This theorem shows that the linear superposition principle holds for the density of the general WKB system (1.1) and (1.2) in the sense that direct summation of all multi-valued densities gives the physical observed density.

Similar results hold for other quantities and is summarized below.

Theorem 4.2 (Superposition Principle for General Function $g(x, p)$). *Let $\{\rho_i\}_{i=1}^N$ be multi-valued densities corresponding to multi-valued fields u_i determined by*

$$u_i \in \{p | \Phi(t, x, p) = 0\},$$

and $g(x, p)$ be any smooth function of x and p . If

$$G = \int f g \delta(\Phi) dp,$$

where f solves (2.7) and Φ solves (2.3) with initial condition (2.4). Then

$$(4.4) \quad G = \sum_{i=1}^N g(x, u_i) \rho_i(t, x).$$

Proof. Following a similar argument to that in the proof of Theorem 4.1, we have

$$\begin{aligned} G(t, x) &= \int_{\mathbb{R}^n} \sigma f g \delta(\Phi) dp, \\ &= \int_{\text{support}(p_i)} f g \frac{\delta(p - p_i)}{|J|} dp. \end{aligned}$$

Use (4.2) again, we obtain

$$(4.5) \quad \begin{aligned} G(t, x) &= \int_{\text{support}(p_i)} \tilde{\rho} |J| g \frac{\delta(p - p_i)}{|J|} dp, \\ &= \tilde{\rho}(t, x, p_i) g(t, x, p_i), \\ &= \rho_i(t, x) g(x, u_i). \end{aligned}$$

This, combined with the partition of unity, gives the asserted (4.4). \square

5. NUMERICAL IMPLEMENTATION

In this section, we summarize our numerical procedures to compute the multi-valued velocity and other quantities. We also verify the superposition property stated in Theorem 4.1 and Theorem 4.2.

Step 1. Discretization and Initialization

We will mostly use uniform mesh size $(\Delta x, \Delta p)$ in x and p . The determination of the computation domain heavily relies on the bi-characteristic whenever possible. The guideline is that it shall cover the range of velocity in p direction and contains at least one period of initial velocity in x if given periodic initial data. By choosing large enough computation domain, we mostly use periodic boundary condition in the simulation.

Step 2. Solve the level set equation (2.3) for Φ and equation (2.7) of f .

The transport equation (2.3) and (2.7) can be reduced into the form

$$\frac{d\Phi^{ij}(t)}{dt} = -H_p^{ij}(t)\Phi_x^{ij}(t) + H_x^{ij}(t)\Phi_p^{ij}(t) := \mathcal{P}(\Phi^{ij}(t)),$$

where $H^{ij}(t)$ and $\Phi^{ij}(t)$ is the numerical approximation of H and ϕ at node (t, x_i, p_j) . Usually, H_p and H_x are given explicitly and Φ_x, Φ_p can be approximated by r^{th} order ENO scheme [12, 13, 25, 28, 30]. In our simulation, second order ENO approximation is applied.

Then, for time discretization we use second order SSP Runge-Kutta method [11],

$$\begin{aligned} k^{ij} &= \Phi^{ij}(t) + \Delta t \mathcal{P}(\Phi^{ij}(t)), \\ (5.1) \quad \Phi^{ij}(t + \Delta t) &= \frac{1}{2}\Phi^{ij}(t) + \frac{1}{2}(k^{ij} + \Delta t \mathcal{P}(k^{ij})). \end{aligned}$$

This method is also known as Heun's method, which has been implemented in [29]. However, we refer it as second order SSP Runge-Kutta method, which can be easily extended to higher order schemes in the category of SSP Runge-Kutta method, see in [11].

Step 3. Visualize the multi-valued velocity by project the zero level set of Φ onto $x - p$ space.

In 1D example, for the velocity, we plot out only grid points satisfying

$$\{(x_i, p_j) \in \Omega \mid |\Phi(t, x_i, p_j)| < \epsilon'\},$$

where ϵ' is chosen in such a way that a unique grid point can be identified along the zero level set. Since it is computationally impossible to find the points where Φ are exactly zero, the zero level set of Φ is realized within a small interval of zero, i.e., any points, with function value close enough to zero, will be considered in the zero level set. We point out that a larger ϵ' may be necessary for the case when level set functions are rough.

Step 4. Evaluate the integral (2.8)

$$\bar{\rho}^{int}(t, x) = \int_{\mathbb{R}^n} f \delta(\Phi) dp.$$

Since this integration involves the Dirac δ -function in its integrand, as usual we first regularize the Dirac δ -function by a smooth bounded function δ_ϵ in such a way that $\delta_\epsilon \rightarrow \delta$ as $\epsilon \rightarrow 0^+$. The error introduced in this regularization step depends on the choice of the approximation, whose accuracy is indicated by a so called moment condition [1] of the regularization. δ_ϵ is said to satisfy r^{th} order of moment condition if $\int_{\mathbb{R}} \delta_\epsilon(x) = 1$ and $\int_{\mathbb{R}} \delta_\epsilon(x) x^k = 0$ for $1 \leq k \leq r$. Under the condition that δ_ϵ is sufficiently resolved by the grid, it is known that the higher the order of moment condition, the smaller the regularization error. Otherwise, the concept of discrete moments should be introduced, see e.g. [8]. The choice of regularization δ_ϵ could be any smooth function with the above

properties. However, considering the concentration of the *delta*-function, it suffices to choose δ_ϵ to have a compact support:

$$\delta_\epsilon(x) = \begin{cases} \frac{1}{\epsilon}\Psi\left(\frac{x}{\epsilon}\right), & |x| \leq \epsilon, \\ 0, & |x| > \epsilon. \end{cases}$$

One of the well accepted choices of this type of δ_ϵ is the cosine kernel, $\Psi(\eta) = \frac{1}{2}(1 + \cos(\pi\eta))$, i.e.,

$$(5.2) \quad \delta_\epsilon^{\text{cos}}(x) = \frac{1}{2\epsilon} \left(1 + \cos\left(\frac{\pi x}{\epsilon}\right)\right) I_{[-\epsilon, \epsilon]},$$

which has first order moment condition. Here $I_{[-\epsilon, \epsilon]}$ is the standard indicator function.

Replacing $\delta(\Phi)$ by $\delta_\epsilon(\Phi)$, we thus have the first approximation of $\bar{\rho}$,

$$(5.3) \quad \bar{\rho}_\epsilon^{\text{int}}(t, x) = \int_{\mathbb{R}} f(t, x, p,) \delta_\epsilon(\Phi) dp,$$

to which standard quadrature rules can be applied. In our simulation, the rectangle rule is chosen and the numerical density is further evaluated by

$$(5.4) \quad \bar{\rho}_{\epsilon h}^{\text{int}}(t, x) = \sum_{\{|\Phi(t, x, p_j)| \leq \epsilon\}} f(t, x, p_j) \delta_\epsilon^{\text{cos}}(\Phi) \Delta p.$$

In this two-step procedure, total error is bounded by the sum of regularization error $|\bar{\rho}^{\text{int}} - \bar{\rho}_\epsilon^{\text{int}}|$ and quadrature error $|\bar{\rho}_\epsilon^{\text{int}} - \bar{\rho}_{\epsilon h}^{\text{int}}|$. For example, if the cosine kernel and the rectangle rule are used, $|\bar{\rho}^{\text{int}} - \bar{\rho}_\epsilon^{\text{int}}|$ is of order ϵ and $|\bar{\rho}_\epsilon^{\text{int}} - \bar{\rho}_{\epsilon h}^{\text{int}}|$ is of order h/ϵ , where $h = \max\{\Delta p\}$. Then the optimal ϵ would be order of \sqrt{h} , which leads to order of \sqrt{h} in total error. In the simulation, ϵ is tested with a range of quantities proportional to h , i.e., $\epsilon = mh$, $m = 1, 2, \dots$. See [8, 22, 27, 31] for details on the error analysis of approximating δ -functions. Keeping a constant ratio between h and ϵ may lead to inconvergence, as pointed out in [8].

Step 5. Computation of multi-valued density $\{\rho_i\}$.

In general, we compute the multi-valued density by (3.4) and the detailed algorithm is discussed in §3. This approach will work for general systems. However, in cases where $\Gamma = \nabla_\alpha x(t, \alpha)$ can be explicitly expressed in terms of α and t , we choose to use formula (3.6), i.e.,

$$\rho(t, x(t, \alpha)) = \frac{\rho_0(\alpha)}{|\det(\Gamma)|}.$$

This formula gives a parameterized solution in terms of α and thus can be used to plot the contour of ρ in $x - \rho$ space. Then interpolation should be used. In simulation, we first discretize α into nodes $\{\alpha_k \mid k = 1, 2, \dots\}$ and compute $(x(t, \alpha_k), \rho(t, x(t, \alpha_k)))$. Then linear interpolation is used locally for any points wherever function values are needed. In this manner, $\rho(t, x)$ can be evaluated at any point x_i . Note that, in our simulation we will utilize this formula (3.6) to compute exact multi-valued solution whenever available.

Step 6. Verify the superposition by comparing $\bar{\rho}_{\epsilon h}^{\text{int}}$ and $\bar{\rho} := \sum_i^N \rho_i$ using both figures and tables of L^1 errors. Here and after, we will refer $\bar{\rho}_{\epsilon h}^{\text{int}}$ and $\sum_i^N \rho_i$ as the results from integral and superposition respectively.

In one dimension with uniform mesh size in x , the L^1 error for $\bar{\rho}$ is defined by

$$Error_{\bar{\rho}} = \sum_{x_i} |\rho_{ch}^{int}(t, x_i) - \bar{\rho}(t, x_i)| \Delta x,$$

where $\rho_{ch}^{int}(t, x_i)$ and $\bar{\rho}(t, x_i)$ are defined by (4.1) and (5.4). Similar definitions apply to other quantities of interest.

6. NUMERICAL EXAMPLES

6.1. The Schrödinger equation. In this example, the Hamiltonian is of the form

$$H(x, p) = \frac{1}{2}|p|^2 + V,$$

which arises in the semi-classical limits of the Schrödinger equation (1.5).

In this case, we are interested in density ρ , and the quantities when $g_1 = \nabla_p H$ and $g_2 = H$. Actually, these two functions g_1 and g_2 correspond to the momentum

$$\bar{J} = \int |p| f \delta(\Phi) dp$$

and energy

$$\bar{E} = \int \left(\frac{1}{2}|p|^2 + V\right) f \delta(\Phi) dp.$$

We have already shown in §4 that all these three quantities can be calculated from those multi-valued u_i and ρ_i . Now we make numerical comparison of the averaged quantities computed from two approaches, integration or superposition. Note here that in order to use superposition, we have two ways to prepare the multi-valued density, which includes (3.6) and (3.4). (3.6) is used whenever the ODE system (2.1) can be solved explicitly.

(1) Example 1: 1D and $V = 0$

$$\begin{aligned} u_0 &= -\sin(\pi x), \\ \rho_0 &= \exp(-(x - 0.5)^2). \end{aligned}$$

This example was used in [10]. Throughout the numerical simulation, unless otherwise specified, second order ENO and second order SSP Runge-Kutta methods are used. The CFL number is taken to be 0.95 to ensure the time efficiency. Here and after, for the density, circle denotes the numerical results from level set method (2.7) and integration (5.4), and this is further noted as results from integration. Meanwhile, solid lines represents the results from either ODE system (3.6) and superposition (4.1), whenever the ODE system can be solved explicitly, or level set method (2.7), multi-valued density (3.4) and superposition (4.1). This is further referred to results from superposition. Similar notation are used for the representations of other quantities as well. In this simulation, computation domain are $[-1, 1] \times [-1.5, 1.5]$ with step sizes (0.02, 0.02) and time at about 0.1, 0.3 and 0.6. The multi-valued density is computed by (3.6), since the problem is potential free and the exact parametric solution can be written down explicitly. Here, periodic and constant boundary conditions are used in solving for velocity and f , respectively. That is we assuming the velocity is periodic while the density are flat outside our computation domain.

From Fig.1, Fig.2 and Fig.3, we can clearly see the capacity of our method. Before singularity—when system develops multi-valuedness, two results are the same and after singularity, peaks in all the three quantities are well captured, i.e., the circle goes up when there is a peak in the solid line.

Table 1 shows the L^1 error for the averaged density $\bar{\rho}$, momentum \bar{J} and energy \bar{E} , which correspond to the quantities defined in Theorem 4.2 with $g = 1$ and $g = p$ and $g = |p|^2/2$ respectively. Moreover, we also notice that there is an optimal ϵ as we pick different m in $\epsilon = mh$. At time 0.101333 the errors in $\bar{\rho}$, \bar{J} and \bar{E} are of order 10^{-2} , 10^{-4} and 10^{-4} respectively with step size at $\Delta x = 0.02$ and $\Delta p = 0.02$ at the optimal ϵ . After singularity we still get very good resolution as seen in Fig.2 and Fig.3.

We also notice the effect of integration support ϵ on the error. Before multi-valued solution appears, the larger the size of the support ϵ tends to give better accuracy, due to the smoothness of the solution. We can see this from the errors for the average density, momentum and energy at time 0.101333 in Table 1. In the case under consideration $\epsilon = mh$ when $m = 4$ gives better results in our integration approximation. However, after the formation of multi-valuedness, we have to pick smaller ϵ .

We then refine our mesh size to be $[0.01, 0.01]$, and similar observation is also made in Table 2. When we further refine the mesh size to be $[0.005, 0.005]$, before singularity the error can be seen in Table 3. However, after singularity, we have to use very small integration support say $1h$, see in Table 4. The figures are much similar to what we obtained by coarse mesh and hence not presented here. Similar phenomenon is also observed in the following examples.

Finally, we make a special remark on the distribution of circles in the multi-valued velocity. In the up-left sub-figures in Fig.2 and Fig.3, where we observe uneven distributions of circles. This is largely caused by the projection of Φ onto its zero level set. Since the zero level set of Φ doesn't always go through our computational grid points, we can only pick out those which are very close to grid points. This lack of continuity in multi-valued velocity can be improved by choosing finer grids.

(2) Example 2: 1D and $V = 0$

$$\begin{aligned} u_0 &= -\sin(\pi x)|\sin(\pi x)|, \\ \rho_0 &= \exp(-(x - 0.5)^2), \end{aligned}$$

which was used in [10].

At time about 0.1, 0.4 and 0.8 with step size $[0.02, 0.02]$ we use second order ENO and second SSP Runge-kutta method, see Fig.4, Fig.5 and Fig.6. In this example, the multi-valued density is computed by (3.6).

In Fig.4, Fig.5 and Fig.6, we notice that the results from level set method and the one from Theorem 4.2 match quite well. Especially, before singularity, the result from level set method are very accurate, which is shown in Table 5. At time 0.101333 the errors in $\bar{\rho}$, \bar{J} and \bar{E} are of order 10^{-2} , 10^{-4} and 10^{-4} respectively with step size at $\Delta x = 0.02$ and $\Delta p = 0.02$. After singularity we still get very good resolution as in Fig.5 and Fig.6. we still use periodic or constant boundary conditions in the case of solving for velocity

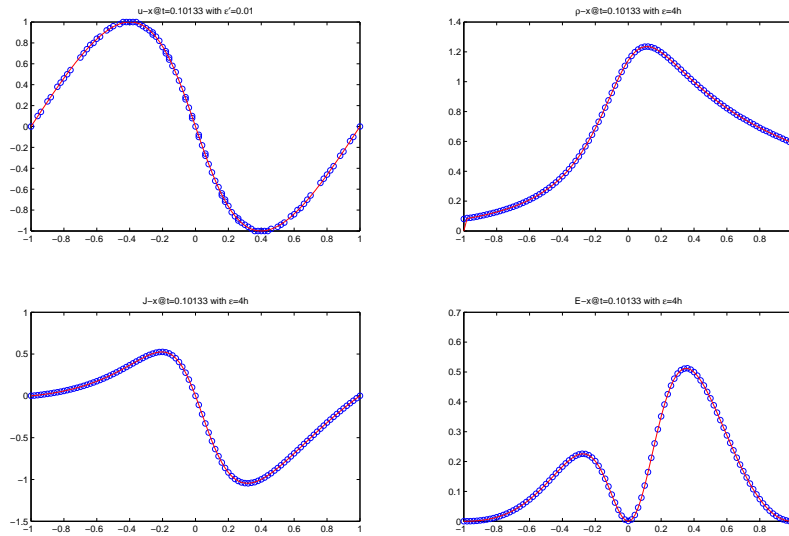


FIGURE 1. Example 1, at $t = 0.101333$. Sub-figures, from up left, are velocity, density, momentum and energy with $\epsilon' = 0.01$ and $\epsilon = 4h$. Circle and solid line represent the results from integration and superposition.

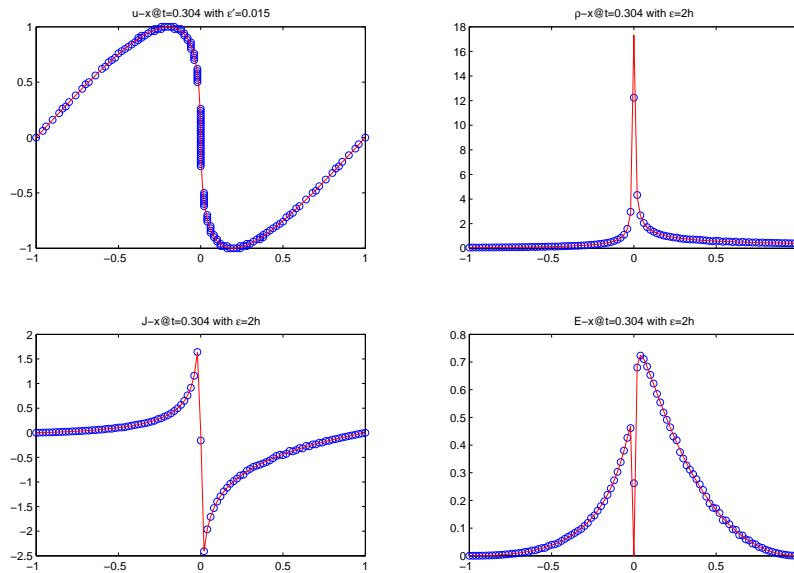


FIGURE 2. Example 1, at $t = 0.304000$. Sub-figures, from up left, are velocity, density, momentum and energy with $\epsilon' = 0.015$ and $\epsilon = 2h$. Circle and solid line represent the results from integration and superposition.

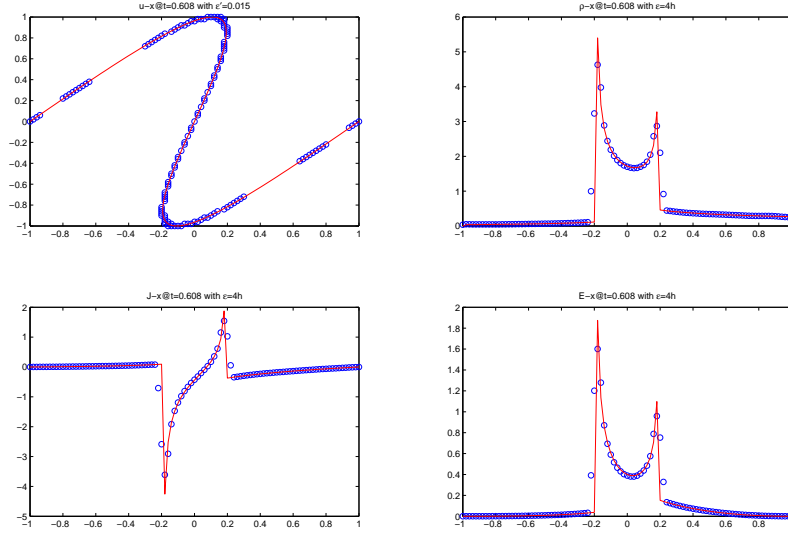


FIGURE 3. Example 1, at $t = 0.608000$. Sub-figures, from up left, are velocity, density, momentum and energy with $\epsilon' = 0.015$ and $\epsilon = 4h$. Circle and solid line represent the results from integration and superposition.

t	$\epsilon = 2h$	$\epsilon = 3h$	$\epsilon = 4h$	$\epsilon = 5h$	$\epsilon = 6h$
0.101333	0.0167394677	0.0135057820	0.0126285789	0.0123750004	0.0122404699
0.304000	0.1293897319	0.1670558597	0.2117553210	0.2512718005	0.2806063519
0.608000	0.2105845480	0.1407095069	0.1774095427	0.2056773509	0.2268914252

1. Error for averaged density $\bar{\rho}$

t	$\epsilon = 2h$	$\epsilon = 3h$	$\epsilon = 4h$	$\epsilon = 5h$	$\epsilon = 6h$
0.101333	0.0034993097	0.0010479213	0.0005364168	0.0004407054	0.0005107636
0.304000	0.0131135016	0.0098454853	0.0143602091	0.0225903714	0.0328003001
0.608000	0.1406452841	0.1122488771	0.1434971805	0.1673175011	0.1849303384

2. Error for averaged momentum \bar{J}

t	$\epsilon = 2h$	$\epsilon = 3h$	$\epsilon = 4h$	$\epsilon = 5h$	$\epsilon = 6h$
0.101333	0.0014676255	0.0005905758	0.0006434041	0.0008985308	0.0012774845
0.304000	0.0092880972	0.0102827107	0.0141035968	0.0162260022	0.0177831562
0.608000	0.0570531980	0.0486087232	0.0624852617	0.0724525964	0.0798224902

3. Error for averaged energy \bar{E}

TABLE 1. Example 1, table of L^1 error for each density, momentum and energy at different time and support size $\epsilon = mh$, $m = 2, 3, 4, 5, 6$ with mesh size $[0.02, 0.02]$.

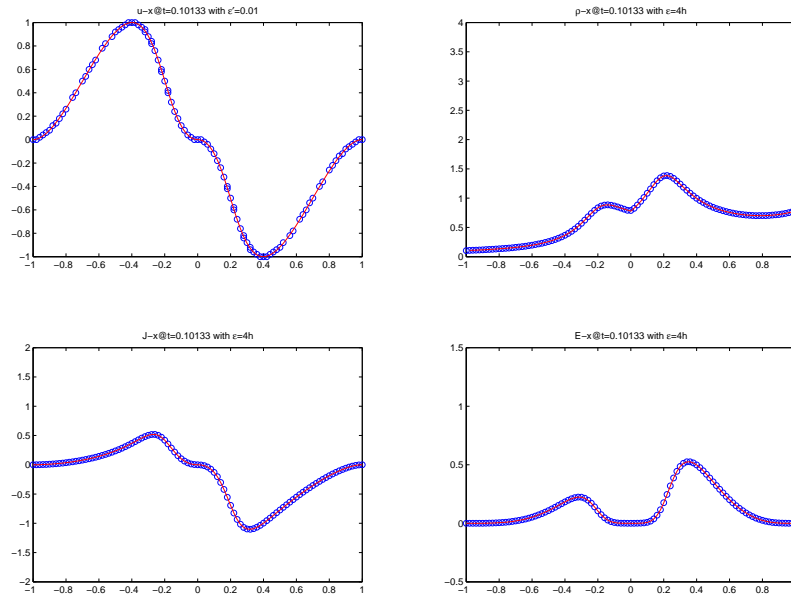


FIGURE 4. Example 2, at $t = 0.101333$. Sub-figures, from up left, are velocity, density, momentum and energy with $\epsilon' = 0.01$ and $\epsilon = 4h$. Circle and solid line represent the results from integration and superposition.

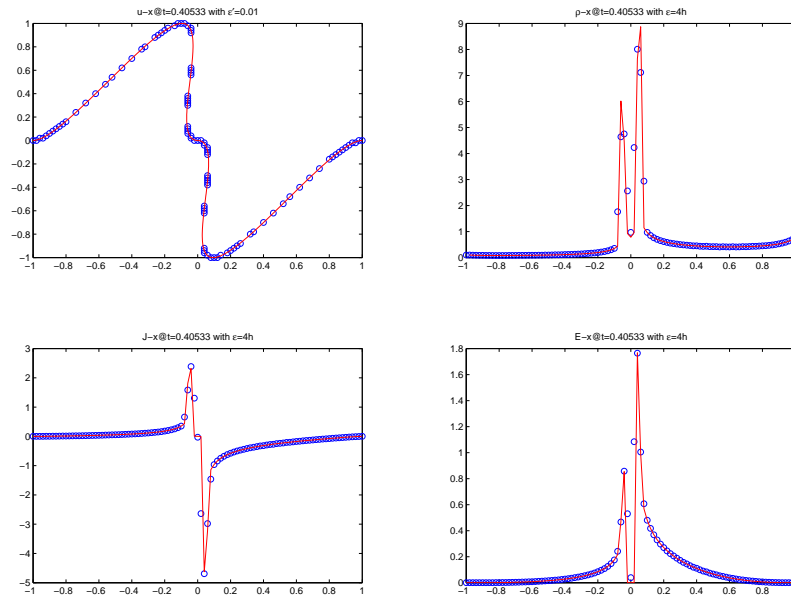


FIGURE 5. Example 2, at $t = 0.405333$. Sub-figures, from up left, are velocity, density, momentum and energy with $\epsilon' = 0.01$ and $\epsilon = 4h$. Circle and solid line represent the results from integration and superposition.

t	$\epsilon = 2h$	$\epsilon = 3h$	$\epsilon = 4h$	$\epsilon = 5h$	$\epsilon = 6h$
0.101333	0.0051376816	0.0017909586	0.0007273995	0.0004612454	0.0002879974
0.304000	0.0401613828	0.0540509632	0.0742904492	0.0939465245	0.1097445398
0.601667	0.1790942828	0.1392930622	0.1715167965	0.2018234660	0.2187257480

1. Error for averaged density $\bar{\rho}$

t	$\epsilon = 2h$	$\epsilon = 3h$	$\epsilon = 4h$	$\epsilon = 5h$	$\epsilon = 6h$
0.101333	0.0037886964	0.0010317342	0.0004580228	0.0002600766	0.0001834229
0.304000	0.0087517411	0.0050335903	0.0062053525	0.0100639636	0.0146909349
0.601667	0.1195325754	0.1245457938	0.1682407453	0.1991976845	0.2142569738

2. Error for averaged momentum \bar{J}

t	$\epsilon = 2h$	$\epsilon = 3h$	$\epsilon = 4h$	$\epsilon = 5h$	$\epsilon = 6h$
0.101333	0.0015507135	0.0004300757	0.0002650783	0.0002767778	0.0003522299
0.304000	0.0044669558	0.0037550843	0.0044664726	0.0054104155	0.0060948187
0.601667	0.0473188337	0.0605047765	0.0904420081	0.1071774789	0.1139000534

3. Error for averaged energy \bar{E}

TABLE 2. Example 1, table of L^1 error for each density, momentum and energy at different time and support size $\epsilon = mh$, $m = 2, 3, 4, 5, 6$ with mesh size $[0.01, 0.01]$.

t	$\epsilon = 2h$	$\epsilon = 3h$	$\epsilon = 4h$	$\epsilon = 5h$	$\epsilon = 6h$
0.101333	0.0054255900	0.0019348151	0.0007616662	0.0004350618	0.0002721383
0.300833	0.0186806191	0.0147565168	0.0193886939	0.0388620747	0.0582130475

1. Error for averaged density $\bar{\rho}$

t	$\epsilon = 2h$	$\epsilon = 3h$	$\epsilon = 4h$	$\epsilon = 5h$	$\epsilon = 6h$
0.101333	0.0040379382	0.0011509129	0.0005013195	0.0002428330	0.0001554436
0.300833	0.0144889280	0.0096615926	0.0123598190	0.0361839326	0.0600986628

2. Error for averaged momentum \bar{J}

t	$\epsilon = 2h$	$\epsilon = 3h$	$\epsilon = 4h$	$\epsilon = 5h$	$\epsilon = 6h$
0.101333	0.0016727121	0.0004593942	0.0002253712	0.0001354775	0.0001186966
0.300833	0.0079236149	0.0057813211	0.0075974680	0.0246010823	0.0414202958

3. Error for averaged energy \bar{E}

TABLE 3. Example 1, table of L^1 error for each density, momentum and energy at different time before singularity and support size $\epsilon = mh$, $m = 2, 3, 4, 5, 6$ with mesh size $[0.005, 0.005]$.

and f . For the integration support size ϵ , as in Example 1, we also notice that before singularity, ϵ should be larger and after singularity smaller ϵ is preferred.

Quantity	$\epsilon = h$	$\epsilon = 1.5h$	$\epsilon = 2h$	$\epsilon = 2.5h$	$\epsilon = 3h$
$\bar{\rho}$	0.3043520483	0.1102531630	4.2457918328	75.4350338239	137.7567242360
J	0.1683337070	0.0529774237	6.3482644876	113.1095259437	206.5710968736
E	0.0584617304	0.0167521244	4.7568178601	84.8200884047	154.9095826285

TABLE 4. Example 1, table of L^1 error for each density, momentum and energy after singularity at time 0.402167 and support size $\epsilon = mh$, $m = 1, 1.5, 2, 2.5, 3$ with mesh size $[0.005, 0.005]$.

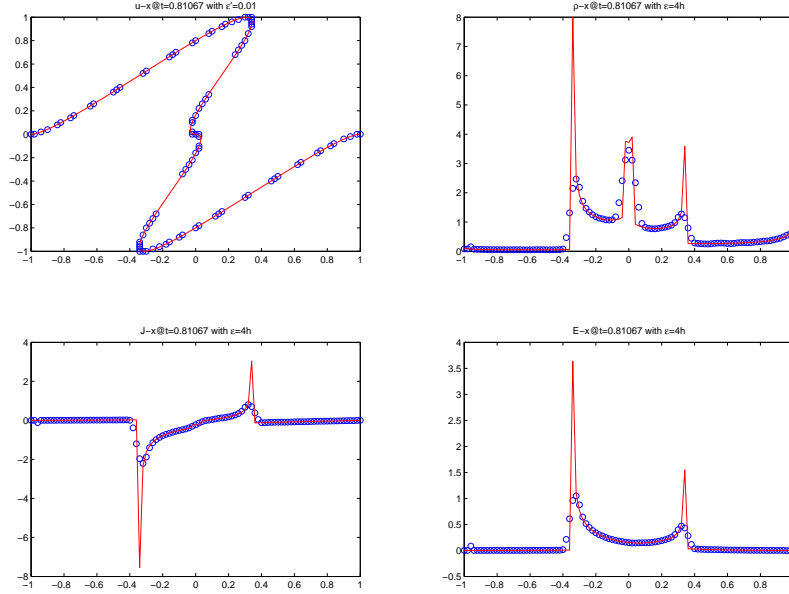


FIGURE 6. Example 2, at $t = 0.810667$. Sub-figures, from up left, are velocity, density, momentum and energy with $\epsilon' = 0.01$ and $\epsilon = 4h$. Circle and solid line represent the results from integration and superposition.

6.2. **Wave equation.** In this section, we test the following Hamiltonian

$$H(x, p) = c(x)|p|, \quad H_p = c(x) \frac{p}{|p|}.$$

This Hamiltonian comes from the WKB expansion of wave equation (1.6).

Now we are still interested in the following quantities

$$\begin{aligned} \bar{\rho} &= \int f \delta(\Phi) dp, \\ \bar{J} &= \int c(x) \frac{p}{|p|} f \delta(\Phi) dp, \\ \bar{E} &= \int c(x) |p| f \delta(\Phi) dp, \end{aligned}$$

t	$\epsilon = 2h$	$\epsilon = 3h$	$\epsilon = 4h$	$\epsilon = 5h$	$\epsilon = 6h$
0.101333	0.0201441257	0.0173173587	0.0163551543	0.0162149049	0.0160895224
0.405333	0.1353771931	0.2096008463	0.2570685836	0.2899839171	0.3458325428
0.810667	0.3638322043	0.3349340467	0.3721443546	0.4093349941	0.4441836011

1. Error for averaged density $\bar{\rho}$

t	$\epsilon = 2h$	$\epsilon = 3h$	$\epsilon = 4h$	$\epsilon = 5h$	$\epsilon = 6h$
0.101333	0.0024015908	0.0008418077	0.0004557995	0.0005120796	0.0006508837
0.405333	0.0824243578	0.1045426391	0.1040800957	0.1170525606	0.1358341234
0.810667	0.2234771392	0.2049319728	0.2283069834	0.2550550387	0.2760111370

2. Error for averaged momentum \bar{J}

t	$\epsilon = 2h$	$\epsilon = 3h$	$\epsilon = 4h$	$\epsilon = 5h$	$\epsilon = 6h$
0.101333	0.0010576917	0.0005229522	0.0006651123	0.0009172565	0.0012734635
0.405333	0.0318257465	0.0377931322	0.0354224554	0.0465411020	0.0560490059
0.810667	0.0973139057	0.0965972571	0.1084100663	0.1206675156	0.1305867870

3. Error for averaged energy \bar{E}

TABLE 5. Example 2, table of L^1 error for each density momentum and energy at different time and support size $\epsilon = mh$, $m = 2, 3, 4, 5, 6$ with step size $[0.02, 0, 02]$.

i.e., with $g = 1$, $g = c(x)\frac{p}{|p|}$ and $g = c(x)|p|$ in Theorem 4.2. Here and after, we call the last two quantities momentum and energy. We now test them by the following examples from [15].

(3) **Example 3: 1D and constant speed** $c(x) = 1$.

$$(6.1) \quad S_0 = -\frac{x^2 - 0.25}{4},$$

$$(6.2) \quad A_0 = \chi_{[-0.7, -0.3] \cup [0.3, 0.7]}(x),$$

where $\rho_0 = A_0^2/c^2$. Here χ_Ω is the characteristic function of Ω .

In this case, we have to solve the level set equation (2.3) for both $H = c|p|$. Since $\nabla_p H = c\frac{p}{|p|}$, undefined at $p = 0$, as in [15] we choose to exclude this singular set in our computation domain. In simulation, we exclude the set

$$\Omega_{exclude} = \{(x, p) \mid |p| < \max_i \Delta p_i, \quad i = 1, 2, \dots, n\},$$

where Δp_i is the step size in p_i direction. The multi-valued density is computed by (3.6). In this example, the initial velocity is $u_0 = -x/2$, which is decreasing. We know that the solution will become multi-valued immediately since the wave with negative speed is on the right and moving towards left, while the wave with positive speed is on the left and moving right.

In the simulation, the mesh size is picked as $[0.02, 0.02]$. In this example, the multi-valued density is computed by (3.6). Constant boundary condition is used in this case. From Fig.(7), Fig.(8) and Fig.(9), we see that those average quantities match nicely, which numerically shows the superposition. Meanwhile the Table 6 of error gives the numerical

t	$\epsilon = 2h$	$\epsilon = 3h$	$\epsilon = 4h$	$\epsilon = 5h$	$\epsilon = 6h$
0.351500	0.1243459867	0.1243459894	0.1243460235	0.1243461163	0.1243450280
0.408500	0.1269397689	0.1269397703	0.1269398218	0.1269404161	0.1269415934
1.007000	0.1667407901	0.1667406964	0.1667402289	0.1667377286	0.1667242841

1. Error for averaged density $\bar{\rho}$

t	$\epsilon = 2h$	$\epsilon = 3h$	$\epsilon = 4h$	$\epsilon = 5h$	$\epsilon = 6h$
0.351500	0.1122599833	0.1122599806	0.1122599464	0.1122595708	0.1122560508
0.408500	0.1260541833	0.1260541819	0.1260541304	0.1260535361	0.1260514986
1.007000	0.1667388478	0.1667387542	0.1667382866	0.1667357863	0.1667223418

2. Error for averaged momentum \bar{J}

t	$\epsilon = 2h$	$\epsilon = 3h$	$\epsilon = 4h$	$\epsilon = 5h$	$\epsilon = 6h$
0.351500	0.0319705467	0.0319439985	0.0319378147	0.0319350105	0.0319335234
0.408500	0.0321329464	0.0321274079	0.0321255184	0.0321246575	0.0321242228
1.007000	0.0428831029	0.0428384220	0.0428303218	0.0428281333	0.0428269787

3. Error for averaged energy \bar{E}

TABLE 6. Example 3, table of L^1 error for each density momentum and energy at different time and support size $\epsilon = mh$, $m = 2, 3, 4, 5, 6$ with step size $[0.02, 0.02]$.

L^1 error of density, momentum and energy at different time and support ϵ . We notice that the error doesn't depend on the support size ϵ . Thus we refined our mesh size to be $[0.01, 0.01]$ and show the L^1 error in Table 7. We could easily see that the error doesn't change with respect to ϵ . Besides mesh refinement, in the next example, same observation is also made.

(4) Example 4: 1D and variable speed $c(x)$

$$(6.3) \quad S_0 = -\frac{x^2}{4},$$

$$(6.4) \quad A_0 = \chi_{[-0.45, -0.25] \cup [0.25, 0.45]}(x),$$

with $c(x) = 3 + 1.5 \tanh(x)$ and $\rho_0 = A_0^2/c^2$.

A similar example was used in [15]. Here, the example taken is a re-scaled one for the save of computation time. Constant boundary condition is used in this case. See the results in Fig.10, Fig.11 and Fig.12. Here, instead of (3.6), the multi-valued density is computed by (3.4)

$$\rho_i \in \left\{ \frac{f}{|\det(\nabla_p \Phi)|} \mid \Phi(t, x, p) = 0 \right\}.$$

Central difference is used to approximate the Jacobian $\nabla_p \Phi$. Then the multi-valued data $\{\tilde{\rho}(t, x_j, u_i), j = 1, \dots, M, i = 1, \dots, N\}$ could be found. Note that those points $\{x_j, j = 1, \dots, M\}$ might not be the same as our grid points from partition of x . Thus, a simple linear interpolation is also used to compute the $\rho(t, x)$ at any grid point x .

From these figures, Fig.10, Fig.11 and Fig.12, we can clearly see the waves crossing and changing its velocity since c is not a constant. Moreover, the error Table 8 shows the L^1

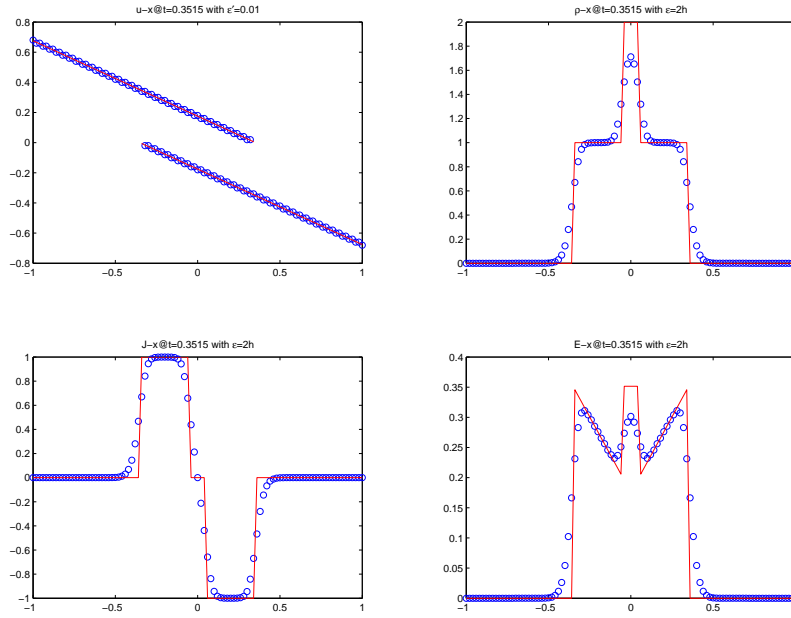


FIGURE 7. Example 3, at $t = 0.3515$. Sub-figures, from up left, are velocity, $g = 1$, $g = \nabla_p H$ and $g = H$ with $\epsilon' = 0.01$ and $\epsilon = 2h$. Circle and solid line represent the results from integration and superposition.

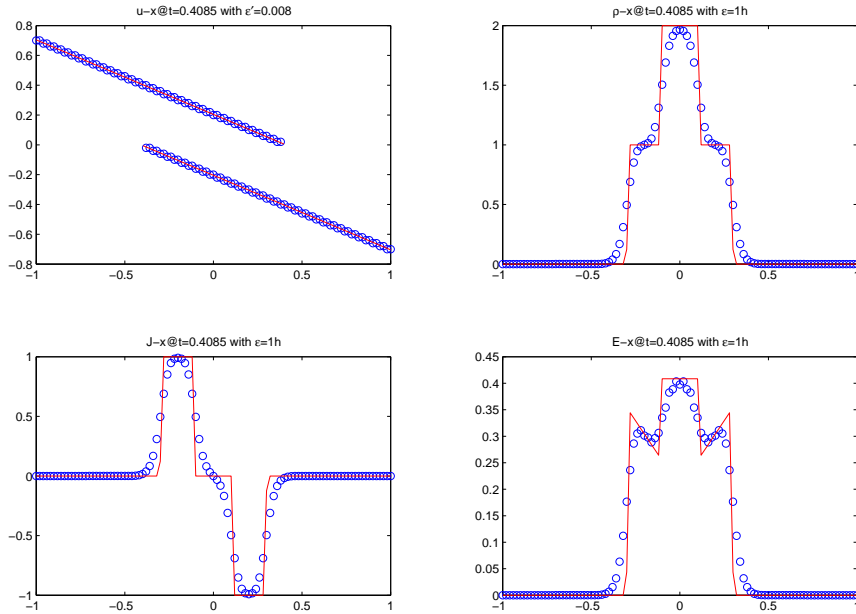


FIGURE 8. Example 3, at $t = 0.408500$. Sub-figures, from up left, are velocity, $g = 1$, $g = \nabla_p H$ and $g = H$ with $\epsilon' = 0.008$ and $\epsilon = h$. Circle and solid line represent the results from integration and superposition.

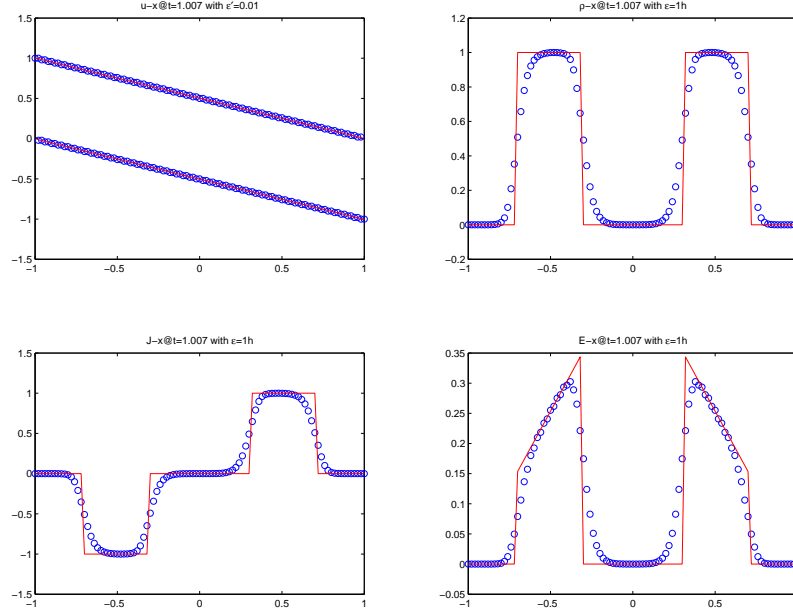


FIGURE 9. Example 3, at $t = 1.00700$. Sub-figures, from up left, are velocity, $g = 1$, $g = \nabla_p H$ and $g = H$ with $\epsilon' = 0.01$ and $\epsilon = h$. Circle and solid line represent the results from integration and superposition.

t	$\epsilon = 2h$	$\epsilon = 3h$	$\epsilon = 4h$	$\epsilon = 5h$	$\epsilon = 6h$
0.351500	0.0730752707	0.0730752707	0.0730752707	0.0730752707	0.0730752707
0.403750	0.0688340482	0.0688340482	0.0688340482	0.0688340482	0.0688340482
1.002250	0.0851973109	0.0851973109	0.0851973109	0.0851973109	0.0851973109

1. Error for averaged density $\bar{\rho}$

t	$\epsilon = 2h$	$\epsilon = 3h$	$\epsilon = 4h$	$\epsilon = 5h$	$\epsilon = 6h$
0.351500	0.0181718495	0.0181535625	0.0181474769	0.0181448518	0.0181435050
0.403750	0.0171266513	0.0171167153	0.0171139650	0.0171129193	0.0171125731
1.002250	0.0217289289	0.0216981950	0.0216887067	0.0216847314	0.0216827964

2. Error for averaged momentum \bar{J}

t	$\epsilon = 2h$	$\epsilon = 3h$	$\epsilon = 4h$	$\epsilon = 5h$	$\epsilon = 6h$
0.351500	0.0027198709	0.0027231238	0.0027322929	0.0027457254	0.0027629154
0.403750	0.0024778875	0.0024666502	0.0024692810	0.0024739515	0.0024868737
1.002250	0.0031984964	0.0031922123	0.0031985274	0.0032105926	0.0032280559

3. Error for averaged energy \bar{E}

TABLE 7. Example 3, table of L^1 error for each density momentum and energy at different time and support size $\epsilon = mh$, $m = 2, 3, 4, 5, 6$ with step size $[0.01, 0.01]$.

t	$\epsilon = 2h$	$\epsilon = 3h$	$\epsilon = 4h$	$\epsilon = 5h$	$\epsilon = 6h$
0.050510	0.0004124339	0.0002574400	0.0002064428	0.0001860470	0.0001836040
0.151460	0.0066038938	0.0065472959	0.0065354958	0.0065220750	0.0065486092
0.252433	0.0005593891	0.0002781005	0.0002250622	0.0002342965	0.0003174496

1. Error for averaged density $\bar{\rho}$

t	$\epsilon = 2h$	$\epsilon = 3h$	$\epsilon = 4h$	$\epsilon = 5h$	$\epsilon = 6h$
0.050510	0.1314190720	0.1314198912	0.1314201536	0.1314201914	0.1314201904
0.151460	0.1070391216	0.1070397427	0.1070394493	0.1070387782	0.1070392338
0.252433	0.1516576004	0.1516669850	0.1516688414	0.1516792368	0.1516929572

2. Error for averaged momentum \bar{J}

t	$\epsilon = 2h$	$\epsilon = 3h$	$\epsilon = 4h$	$\epsilon = 5h$	$\epsilon = 6h$
0.050510	0.0237754984	0.0237694404	0.0237608625	0.0237498011	0.0237362724
0.151460	0.0292403331	0.0292340795	0.0292253946	0.0292141528	0.0292005134
0.252433	0.0249560424	0.0249503050	0.0249415895	0.0249318013	0.0249203468

3. Error for averaged energy \bar{E} TABLE 8. Example 4, table of L^1 error for each density momentum and energy at different time and support size $\epsilon = mh$, $m = 2, 3, 4, 5, 6$

error of the results from integration and superposition. We notice that in this case the error does not depend on the support size ϵ too much.

Remark 1. *In this example 4, numerical error is also introduced by the approximation of $|\det(\nabla_p \Phi)|$. Especially, when u_i coincides with any of computational grids, $|\det(\nabla_p \Phi)| = 0$ and $\rho_i = \infty$ at those points. This could result in huge numerical error. Numerical tests are performed on this issue in two dimensional space, and large error is observed. Thus a new approximation of $|\det(\nabla_p \Phi)|$ is expected in order to use (3.4).*

Remark 2. *From above examples, we notice that the integration support ϵ in (5.2) plays an important role in the error control. Moreover, optimal ϵ depends on the appearance of singularity or multi-valuedness. For some cases with $H = \frac{|p|^2}{2} + V$, the singularity appears in finite time, so optimal ϵ is larger before singularity and smaller after singularity formation. For some cases with $H = c|p|$, the multi-valued solution appears immediately, the choice of ϵ does not affect the error much, which can be observed in Table 6 and 8. This phenomenon doesn't change during mesh refinement as seen in Table 2 and 7. The reason for those observations could be that, if multi-valued u 's, say u_i and u_{i+1} , are close, then ϵ is better to be small to avoid the overlap of the support in the numerical integration.*

APPENDIX

Here we justify the formula (3.6)

$$(A.1) \quad \rho(t, x(t, \alpha)) = \frac{\rho_0(\alpha)}{|\det(\Gamma)|},$$

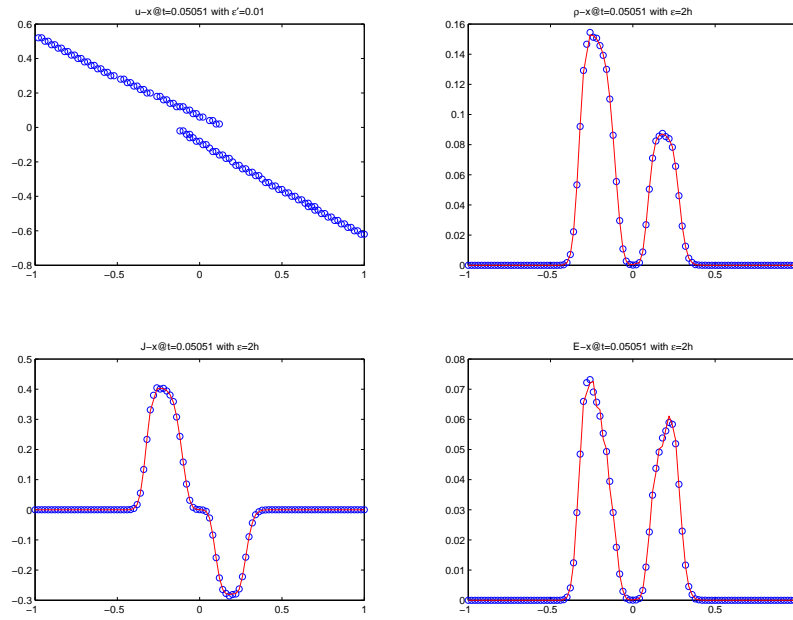


FIGURE 10. Example 4, at $t = 0.05051$. Sub-figures, from up left, are velocity, $g = 1$, $g = \nabla_p H$ and $g = H$ with $\epsilon' = 0.01$ and $\epsilon = 2h$. Circle and solid line represent the results from integration and superposition.

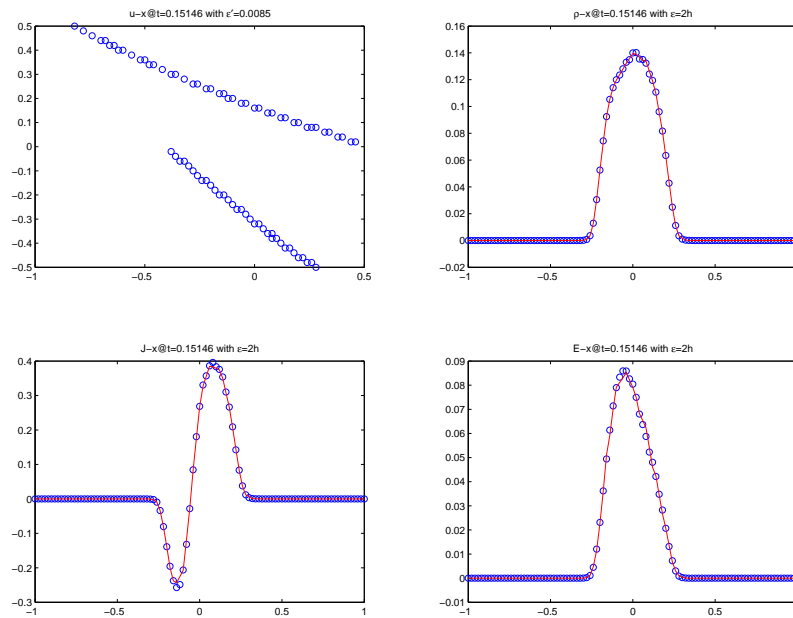


FIGURE 11. Example 4, at $t = 0.15146$. Sub-figures, from up left, are velocity, $g = 1$, $g = \nabla_p H$ and $g = H$ with $\epsilon' = 0.0085$ and $\epsilon = 2h$. Circle and solid line represent the results from integration and superposition.

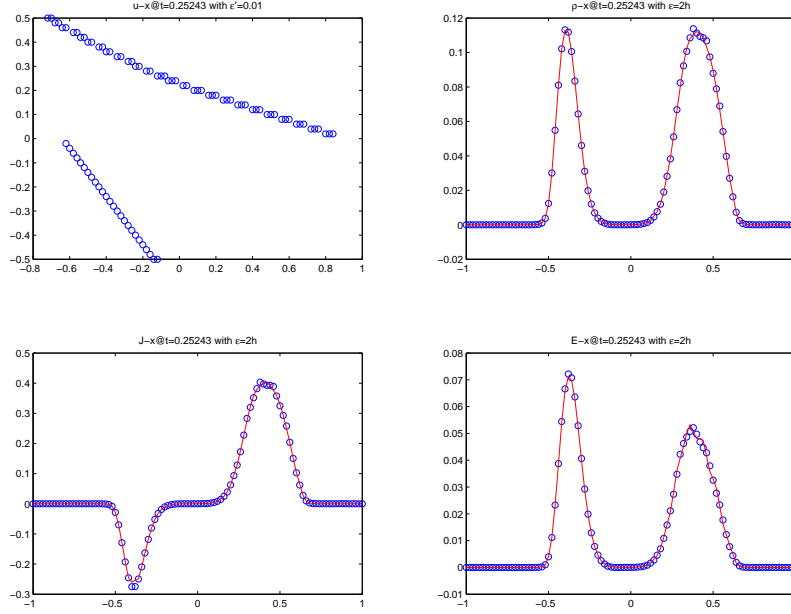


FIGURE 12. Example 4, at $t = 0.25243$. Sub-figures, from up left, are velocity, $g = 1$, $g = \nabla_p H$ and $g = H$ with $\epsilon' = 0.01$ and $\epsilon = 2h$. Circle and solid line represent the results from integration and superposition.

where $x = x(t, \alpha)$ is the characteristics satisfying $\frac{dx}{dt} = \nabla_p H|_{p=\nabla_x S}$, and $\Gamma = \frac{\partial x(t, \alpha)}{\partial \alpha}$. Let $J = \det\left(\frac{\partial x}{\partial \alpha}\right)$, then

$$\frac{\partial J}{\partial t} = \frac{\partial}{\partial t} \det\left(\frac{\partial x_i}{\partial \alpha_j}(t, \alpha)\right) = \sum_{i,j} A_i^j \frac{\partial}{\partial t} \frac{\partial x_i}{\partial \alpha_j}(t, \alpha),$$

where A_i^j is the minor of the element $\frac{\partial x_i}{\partial \alpha_j}$ of the matrix $\frac{\partial x}{\partial \alpha}$.

The minors satisfies

$$\sum_j \frac{\partial x_k}{\partial \alpha_j} A_i^j = \delta_i^k J, \quad \delta_i^k = \begin{cases} 1 & k = i, \\ 0 & k \neq i. \end{cases}$$

Thus the use of the equation $\frac{dx}{dt} = \nabla_p H$ gives

$$\begin{aligned} \frac{\partial J}{\partial t} &= \sum_{i,j} A_i^j \frac{\partial}{\partial \alpha_j} \frac{\partial}{\partial t} x_i = \sum_{i,j} A_i^j \frac{\partial}{\partial \alpha_j} (\partial_{p_i} H) \\ &= \sum_{i,j,k} A_i^j \frac{\partial x_k}{\partial \alpha_j} \left(\frac{\partial}{\partial x_k} (\partial_{p_i} H) \right) = \sum_i \frac{\partial}{\partial x_i} (\partial_{p_i} H) J \\ &= \nabla_x \cdot (\nabla_p H) J. \end{aligned}$$

For any domain Ω , the change of variables $\alpha \rightarrow x(t, \alpha)$ leads to

$$\int_{x(t, \Omega)} \rho(t, x) dx = \int_{\Omega} \rho(t, x(t, \alpha)) J d\alpha,$$

This, by differentiation in t , gives

$$\begin{aligned}
\frac{d}{dt} \int_{x(t,\Omega)} \rho(t,x) dx &= \int_{\Omega} (\rho_t + \frac{dx}{dt} \cdot \nabla_x \rho) J + \rho \frac{\partial J}{\partial t} d\alpha \\
&= \int_{\Omega} (\rho_t + H_p \cdot \nabla_x \rho) J + \rho \nabla_x \cdot \nabla_p H J d\alpha \\
&= \int_{\Omega} [\rho_t + \nabla_x \cdot (\rho \nabla_p H)] J d\alpha \\
&= \int_{x(t,\Omega)} (\rho_t + \nabla_x \cdot (\rho \nabla_p H)) dx \\
&= 0.
\end{aligned}$$

Therefore, we obtain

$$\int_{x(t,\Omega)} \rho(t,x) dx = \int_{\Omega} \rho_0(\alpha) d\alpha.$$

Since this holds for any Ω , we must have

$$\rho(t, x(t, \alpha)) J = \rho_0(\alpha),$$

which gives (A.1), except for the absolute sign on J , which is needed to ensure positivity of the density after singularity.

ACKNOWLEDGMENTS

This research was supported by the National Science Foundation under Grant DMS05-05975.

REFERENCES

- [1] R. P. Beyer and R. J. LeVeque. Analysis of a one-dimensional model for the immersed boundary method. *SIAM J. Numer. Anal.*, 29(2):332–364, 1992.
- [2] Y. Brenier and L. Corrias. A kinetic formulation for multi-branch entropy solutions of scalar conservation laws. *Ann. Inst. H. Poincaré Anal. Non Linéaire*, 15(2):169–190, 1998.
- [3] L.-T. Cheng. Efficient level set methods for constructing wave fronts in three dimensions. UCLA CAM report, 2006.
- [4] L.-T. Cheng, H. Liu, and S. Osher. Computational high-frequency wave propagation using the level set method, with applications to the semi-classical limit of Schrödinger equations. *Commun. Math. Sci.*, 1(3):593–621, 2003.
- [5] M. G. Crandall and P.-L. Lions. Viscosity solutions of Hamilton-Jacobi equations. *Trans. Amer. Math. Soc.*, 277(1):1–42, 1983.
- [6] B. Engquist and O. Runborg. Multi-phase computations in geometrical optics. *J. Comput. Appl. Math.*, 74(1-2):175–192, 1996. TICAM Symposium (Austin, TX, 1995).
- [7] B. Engquist and O. Runborg. Computational high frequency wave propagation. In *Acta numerica, 2003*, volume 12 of *Acta Numer.*, pages 181–266. Cambridge Univ. Press, Cambridge, 2003.
- [8] B. Engquist, A.-K. Tornberg, and R. Tsai. Discretization of Dirac delta functions in level set methods. *J. Comput. Phys.*, 207(1):28–51, 2005.
- [9] L. Gosse. Using K -branch entropy solutions for multivalued geometric optics computations. *J. Comput. Phys.*, 180(1):155–182, 2002.
- [10] L. Gosse, S. Jin, and X. Li. Two moment systems for computing multiphase semiclassical limits of the Schrödinger equation. *Math. Models Methods Appl. Sci.*, 13(12):1689–1723, 2003.

- [11] S. Gottlieb, C.-W. Shu, and E. Tadmor. Strong stability-preserving high-order time discretization methods. *SIAM Rev.*, 43(1):89–112 (electronic), 2001.
- [12] A. Harten. Preliminary results on the extension of ENO schemes to two-dimensional problems. In *Nonlinear hyperbolic problems (St. Etienne, 1986)*, volume 1270 of *Lecture Notes in Math.*, pages 23–40. Springer, Berlin, 1987.
- [13] A. Harten. ENO schemes with subcell resolution. *J. Comput. Phys.*, 83(1):148–184, 1989.
- [14] S. Jin and X. Li. Multi-phase computations of the semiclassical limit of the Schrödinger equation and related problems: Whitham vs. Wigner. *Phys. D*, 182(1-2):46–85, 2003.
- [15] S. Jin, H. Liu, S. Osher, and R. Tsai. Computing multi-valued physical observables for the high frequency limit of symmetric hyperbolic systems. *J. Comput. Phys.*, 210(2):497–518, 2005.
- [16] S. Jin, H. Liu, S. Osher, and Y.-H. R. Tsai. Computing multivalued physical observables for the semiclassical limit of the Schrödinger equation. *J. Comput. Phys.*, 205(1):222–241, 2005.
- [17] S. Jin and S. Osher. A level set method for the computation of multivalued solutions to quasi-linear hyperbolic PDEs and Hamilton-Jacobi equations. *Commun. Math. Sci.*, 1(3):575–591, 2003.
- [18] S. N. Kružkov. First order quasilinear equations with several independent variables. *Mat. Sb. (N.S.)*, 81 (123):228–255, 1970.
- [19] H. Liu, L.-T. Cheng, and S. Osher. A level set framework for capturing multi-valued solutions to nonlinear first-order equations. *J. Comput. Phys.*, 2005.
- [20] H. Liu, S. Osher, and R. Tsai. Multi-valued solution and level set methods in computational high frequency wave propagation. *Commun. Comput. Phys.*, 1(5):765–804, 2006.
- [21] H. Liu and Z. Wang. Computing multi-valued velocity and electric fields for 1d euler-poisson equations. *To appear in APPNUM*, 2006.
- [22] H. Liu and Z. Wang. A field-space based level set method for computing multi-valued solutions to 1d euler-poisson equations. *Accepted by J. Comput. Phys.*, 2006.
- [23] C. Min. Local level set method in high dimension and codimension. *J. Comput. Phys.*, 200(1):368–382, 2004.
- [24] S. Osher, L.-T. Cheng, M. Kang, H. Shim, and Y.-H. Tsai. Geometric optics in a phase-space-based level set and Eulerian framework. *J. Comput. Phys.*, 179(2):622–648, 2002.
- [25] S. Osher and C.-W. Shu. High-order essentially nonoscillatory schemes for Hamilton-Jacobi equations. *SIAM J. Numer. Anal.*, 28(4):907–922, 1991.
- [26] D. Peng, B. Merriman, S. Osher, H. Zhao, and M. Kang. A PDE-based fast local level set method. *J. Comput. Phys.*, 155(2):410–438, 1999.
- [27] P.-A. Raviart. On the numerical analysis of particle simulations in plasma physics. In *Nonlinear partial differential equations and their applications. Collège de France Seminar, Vol. IV (Paris, 1981/1982)*, volume 84 of *Res. Notes in Math.*, pages 173–193. Pitman, Boston, Mass., 1983.
- [28] C.-W. Shu. High order ENO and WENO schemes for computational fluid dynamics. In *High-order methods for computational physics*, volume 9 of *Lect. Notes Comput. Sci. Eng.*, pages 439–582. Springer, Berlin, 1999.
- [29] C.-W. Shu and S. Osher. Efficient implementation of essentially nonoscillatory shock-capturing schemes. *J. Comput. Phys.*, 77(2):439–471, 1988.
- [30] C.-W. Shu and S. Osher. Efficient implementation of essentially nonoscillatory shock-capturing schemes. II. *J. Comput. Phys.*, 83(1):32–78, 1989.
- [31] J. Towers. Two methods for discretizing a delta function supported on a level set. *J. Comput. Phys.* 220 (2007), no. 2, 915–931.
- [32] G. B. Whitham. *Linear and nonlinear waves*. Wiley-Interscience [John Wiley & Sons], New York, 1974. Pure and Applied Mathematics.

IOWA STATE UNIVERSITY, MATHEMATICS DEPARTMENT, AMES, IA 50011

E-mail address: hliu@iastate.edu